Compressible Lifting Surface Theory for Propeller Performance Calculation

Donald B. Hanson*
Hamilton Standard, Windsor Locks, Connecticut

A new integral equation for propeller steady aerodynamic analysis is presented that generalizes wing kernel function methods to include effects of rotation and multiple blades. The kernel of the integral equation is valid in a single form for the case, typical of propfans (advanced technology, many bladed propellers which operate at high cruise Mach number), where the blade section relative speeds are subsonic at the roots and supersonic at the tips. Within the restrictions of linearized theory, effects of blade interference, sweep, three dimensionality, and compressibility are rigorously accounted for. Behavior of the kernel is studied and compared with well-known results from wing and propeller wake theories. Methods for inverting the integral equation to compute lift distribution and for determining vortex (or induced) drag are adapted from wing theory. Computed efficiency, power, and spanwise power distribution are in excellent agreement with data for a propfan model with swept blades tested at 0.8 cruise Mach number in a NASA wind tunnel.

Nomenclature

a	$=\pi/J$
B	= number of blades
B_D	= chord-to-diameter ratio, $=b/2r_T$
c_0	= ambient sound speed
C_D	= drag coefficient
C_L	= lift coefficient
$C_{\hat{n}}$	= shape factor for chordwise loading
C_P	= power coefficient
ΔC_p	= coefficient of lift pressure
$G_{\hat{m}}$	= chordwise distribution factor for control point
i	= spanwise control point index
I_n, K_n	= modified Bessel functions
j	= mode index for spanwise loading
J	= advance ratio, π times flight speed/tip rotational speed
J_n, Y_n	= Bessel functions of first kind
k	= wave number variable
K_L	= kernel function
$\bar{K}_{\mu\nu}$	= integrated kernel function
L_ν	= vector of load coefficients
m	= summation index
$\hat{m}$	= chordwise control point index
M	= forward flight Mach number
$\hat{n}$	= chordwise load point index
r_T	= tip radius
R_j	= spanwise mode shape
w	= induced downwash velocity
W_μ	= downwash angle at μth control point
z, z_0	= control and load radius, respectively, (normalized by r_T)
z_h	= normalized radius at centerbody
$z_<, z_>$	= lesser and greater, respectively, of z_0 and z
β	$=\sqrt{1-M^2}$
Γ_0, Γ	= chordwise position of load and control points, respectively, (divided by r_T) measured in advance direction at constant radius
Γ_L, Γ_T	= values of Γ_0 at leading and trailing edges, respectively
η	= apparent efficiency
μ	= control point index
ν	= load point index
ρ_0	= ambient density
σ, σ_0	$=\sqrt{1+a^2z^2}$ and $\sqrt{1+a^2z_0^2}$, respectively

Presented as Paper 82-0020 at the AIAA 20th Aerospace Sciences Meeting, Orlando, Fla., Jan. 12-14, 1982; received Aug. 1, 1983; revision received June 4, 1984.

*Principal Research Engineer, Design Department, Aircraft Systems Division. Member AIAA.

Introduction

THE aerodynamic design of high-performance airplane propellers has been accomplished over the years with a variety of lifting line methods. Considering the geometry of a typical conventional propeller, shown in Fig. 1, the lifting line approach does not seem unreasonable. However, with the emergence of the propfan, shown in Fig. 2, the simplifying approximations of lifting line theory no longer appear adequate. The blades have low aspect ratio, are strongly swept, and produce a high disk loading because of their large number. Furthermore, at a design cruise speed of Mach 0.8, the section relative Mach numbers may vary from 0.85 in the root area to 1.15 at the tip. Theory to analyze performance, acoustics, and unstalled flutter of propellers with these geometry and flow features was derived in Ref. 1. The present paper is a study of the performance branch of the theory and presents calculations for the SR-3 propfan. The work was motivated not only by the need for better aerodynamic design information but also by the requirement for reliable pressure distribution predictions for structural and acoustic calculations.

In its present form, the theory is compressible and linearized. Linearization was justified in principle in Ref. 1 by the fact that propfan blades satisfy textbook criteria for use of linear theory at transonic speeds by virture of low thickness ratio (2%) and low aspect ratio (3-4). Sweep is an additional benefit in linearizing the flow. Initial results shown herein indicate that linearization is justified, but final judgement must await more detailed comparison with data.

Other organizations are developing nonlinear theories for propeller steady aerodynamics, including a potential method by Jou[2] and an Euler method by Bober et al.[3] A transonic small-disturbance method is also in progress, but no publications are yet available. Ultimately these should be more accurate than any linearized method for transonic blades; however, viscosity has not yet been included and performance maps have not been generated for comparison with test data. The method of this paper includes viscosity simplistically in the form of profile drag looked up in tables of two-dimensional airfoil test data. Agreement between test and predicted performance maps is believed to be the best available at this time. Thus, in its present form, the method can be used inexpensively to determine blade loading for performance estimates, acoustic radiation calculation, and structural purposes. It is not adequate by itself for detailed airfoil section design. As in wing design practice, the linear method may eventually be coupled with one of the more advanced two-dimensional transonic codes. The three-dimensional linear theory would be used to determine the induction and interference, and the two-dimensional theory would be used for details of chordwise distributions.

Another motivation for the present work is that the unsteady version of the theory is needed for analysis of forced response and unstalled flutter. This is a relatively simple extension and currently is being programmed.

In the remainder of the paper, the lifting surface integral equation is presented and the kernel function is studied in detail. The lift and drag calculation methods are then described and sample calculations are given.

Background

In Ref. 1 an integral equation for helicoidal lifting surfaces was derived using the acceleration potential (or pressure potential) method, which required the following steps: An expression for the pressure disturbance caused by helically convected thickness and loading sources was developed using the linear acoustic wave equation

$$\nabla^2 p - \frac{1}{c_0^2}\frac{\partial^2 p}{\partial t^2} = 0 \tag{1}$$

with the free-space Green's function. Helicoidal reference surfaces were defined for each blade so that the usual thin blade approximation could be made and the flow tangency boundary condition could be linearized with respect to them. The helicoids are those swept out by the blade pitch change axes (radii) as they rotate with the propeller and advance at flight Mach number M. In order to establish the velocity potential, the expression for the pressure disturbance (divided by the ambient density to form the acceleraton potential) was integrated along undisturbed streamlines from $-\infty$ to the field (or control) point. Finally, this was differentiated normal to the helicoidal surface to find the upwash caused by the convected sources. In this paper, only the steady lift source is considered; chordwise and spanwise force components are neglected as in most wing lifting surface theories. Theory for the thickness effect was derived in Ref. 1 but has not yet been included in aerodynamic calculations. This restricts the current blade pressure predictions to the difference between upper and lower surface pressures. This blade loading is adequate for structural, acoustic, and induced-drag purposes. However, the upper and lower surface pressures cannot be studied separately.

The integral equation giving the upwash angle induced by the blade pressure distribution is

$$\alpha_i(\Gamma,z) \approx \tan\alpha_i = \int_{z_h}^{1}\int_{\Gamma_L}^{\Gamma_T} \Delta C_p(\Gamma_0,z_0)K_L(\Gamma,z;\Gamma_0,z_0)\,\mathrm{d}\Gamma_0\mathrm{d}z_0 \tag{2}$$

where ΔC_p is the distribution over the blade surface area of the coefficient of lift pressure

$$\Delta C_p = \Delta P/(\tfrac{1}{2}\rho_0 U_0^2) \tag{3}$$

based on local section helical velocity $U_0 = c_0 M\sigma_0$. K_L is the kernel function (or influence coefficient) which gives the induced upwash at the point Γ, z due to a unit load at the point Γ_0, z_0. The blade-fixed streamwise and radial coordinates Γ and z shown in Fig. 3 are normalized by the propeller tip radius r_T and the zero subscripts denote source coordinates. Γ represents distance in the streamwise (or chordwise) direction along an advance helix and is measured at constant radius. (The Γ and z coordinates are nonorthogonal because lines of constant Γ are not radial except for $\Gamma = 0$. As discussed in Ref. 1, this system is desirable and leads to correct results.) For mathematical purposes, the function $\Delta C_p(\Gamma_0, z_0)$ is considered to be defined, but equal to zero for values of Γ_0 less than the leading-edge value Γ_L and greater than the trailing-edge value Γ_T. This convention eliminates

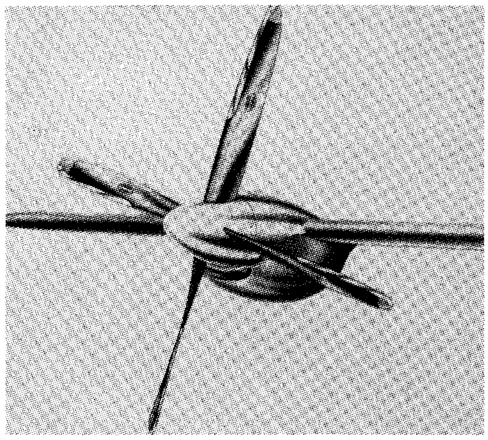

Fig. 1 Conventional propeller with high aspect ratio blades.

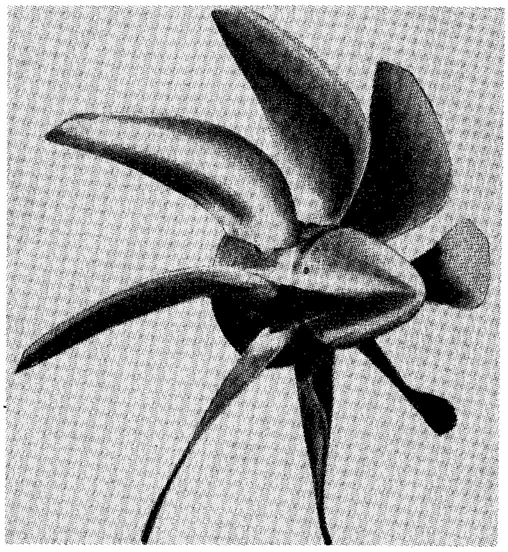

Fig. 2 Propfan propulsor, model SR-3.

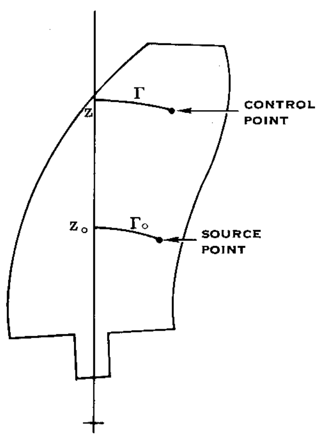

Fig. 3 Source and control point coordinates Γ and Γ_0 are measured at constant radius along advance helix.

some Heaviside step functions that would otherwise appear later in the paper.

The boundary condition to be satisfied is that the flow be tangent to the blade camber surfaces. In terms of Eq. (2), this means, for the analysis problem, that a pressure distribution must be found that induces flow angles equal to the slopes of the blade section camber lines as measured from the helicoidal reference surface. This requires inversion of the integral equation as discussed later. In principle, Eq. (2) could also be used in the direct sense to find the camber surface corresponding to a desired pressure distribution. This is usually known as the design problem and has not yet been pursued.

As written, Eq. (2) could apply to any lifting surface provided the appropriate kernel is supplied. For wings, the kernels are well known[4]:

$$K_{\text{wing}} = \frac{1}{8\pi(z-z_0)^2}\left[1+\frac{\Gamma-\Gamma_0}{\sqrt{(\Gamma-\Gamma_0)^2+\beta^2(z-z_0)^2}}\right] \text{for } M<1 \tag{4a}$$

$$K_{\text{wing}} = \frac{1}{4\pi(z-z_0)^2}\left[\frac{\Gamma-\Gamma_0}{\sqrt{(\Gamma-\Gamma_0)^2+\beta^2(z-z_0)^2}}\right] \quad \text{for } M<1 \tag{4b}$$

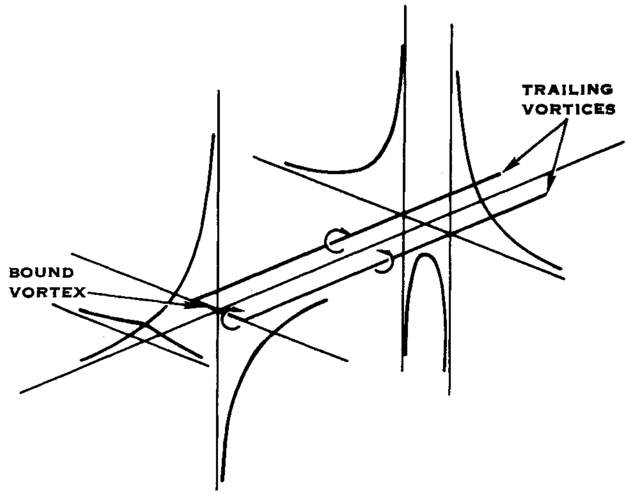

Fig. 4 Horseshoe vortex flowfield.

(For $M>1$, the kernel is taken to be zero when the radicand is negative, i.e., ahead of Mach cones.)

Because of the second-order singularity $(z-z_0)^{-2}$, integrals of Eqs. (4a) and (4b) must be interpreted in the Mangler sense, i.e., as the finite part of an infinite integral.[5] The corresponding kernel for propellers was derived in Ref. 1. After conversion to nondimensional variables, the kernel becomes

$$\begin{aligned} K_L = {} & \frac{Bz_0 z\sigma_0 a^4}{4\pi^2\sigma^2}\int_0^\infty kI_0(a\beta z_< k)K_0(a\beta z_> k)\sin\left[a\left(\frac{\Gamma}{\sigma}-\frac{\Gamma_0}{\sigma_0}\right)k\right]\mathrm{d}k \\ & +\frac{B^3\sigma_0^3}{4\pi z_0 z}\sum_{m=1}^{\infty} m^2 I_{mB}(mBaz_<)K_{mB}(mBaz_>) \\ & -\frac{B^3\sigma_0}{8\pi\sigma^2 z_0 z}\sum_{m=1}^{\infty} m^2\int_{-\infty}^{\infty}\frac{1}{k}[a^2z_0^2(k-1)-1][a^2z^2(k-1)-1](JY)_{mB}\sin\left[mBa\left(\frac{\Gamma}{\sigma}-\frac{\Gamma_0}{\sigma_0}\right)k\right]\mathrm{d}k \\ & -\frac{B^3\sigma_0}{8\pi\sigma^2 z_0 z}\sum_{m=1}^{\infty} m^2\int_{1/(1+M)}^{1/(1-M)}\frac{1}{k}[a^2z_0^2(k-1)-1]\,[a^2z^2(k-1)-1](JJ)_{mB}\cos\left[mBa\left(\frac{\Gamma}{\sigma}-\frac{\Gamma_0}{\sigma_0}\right)k\right]\mathrm{d}k \end{aligned} \tag{5}$$

where

$$(JJ)_{mB} = J_{mB}[mBaz_0\sqrt{M^2k^2-(k-1)^2}\,[J_{mB}]\,mBaz\sqrt{M^2k^2-(k-1)^2}\,] \tag{6a}$$

and

$$\begin{aligned} (JY)_{mB} & = J_{mB}\ [mBaz_<\sqrt{M^2k^2-(k-1)^2}\,]\,Y_{mB}[mBaz_>\sqrt{M^2k^2-(k-1)^2}\,] \qquad \text{for}\ \frac{1}{1-M}\leq k\leq\frac{1}{1+M} \\ & = -\frac{2}{\pi}I_{mB}[mBaz_<\sqrt{(k-1)^2-M^2k^2}\,]K_{mB}[mBaz_>\sqrt{(k-1)^2-M^2k^2}\,] \quad \text{for } |k|\geq\frac{1}{1\pm M} \end{aligned} \tag{6b}$$

Note in the third term of the kernel that the integrand changes form at $k=1/(1+M)$ and at $1/(1-M)$ where $M^2k^2-(k-1)^2$ goes to zero. It happens that the behavior of J_{mB} and Y_{mB} for zero argument is such that $(JY)_{mB}$ is continuous and smooth at these points.

As written, Eq. (5) applies for any subsonic flight Mach number M and any advance ratio $J\neq 0$. For propfans, combinations of M and J occur which lead to section-relative (helical) speeds that are subsonic at the blade roots and supersonic at the tips. Equation (5) has the same form for source and control points in either the subsonic or supersonic regions.

Behavior of Kernel Function

Before developing a method for inverting Eq. (2), it is important to understand the behavior of the kernel function in some detail. Accordingly, this section is devoted to a study of the various terms in Eq. (5) so as to illustrate its behavior near singularities and in the far wake. Also, some computed values of K_L are given to compare its behavior to that of the wing kernel and illustrate effects of compressibility and distributed chord (as opposed to a lifting line).

Properties of Individual Terms

Equation (5) expresses the kernel function as the sum of four terms whose dependence on the streamwise coordinate Γ is explicitly shown. The m summations came from a Fourier series in the circumferential angle. The first term in Eq. (5) is related to the axial induction and has no analog in wing theory.

The second term is analogous to the term $1/8\pi(z-z_0)^2$ in the wing kernel [Eqs. (4)] in that it does not depend on the streamwise variable and does not include compressibility effects (i.e., neither the Mach number nor the Prandtl-Glauert factor β appears). Furthermore, it can be shown that the leading singularity in the second term is exactly $1/8\pi(z-z_0)^2$.

By noting that $\sin(kx)/k$ behaves as a delta function for large x, it can be shown that the third term is exactly equal to the second term for $\Gamma\to-\infty$. This mimics the behavior of $(\Gamma-\Gamma_0)/\sqrt{(\Gamma-\Gamma_0)^2+\beta^2(z-z_0)^2}$ in the wing kernel.

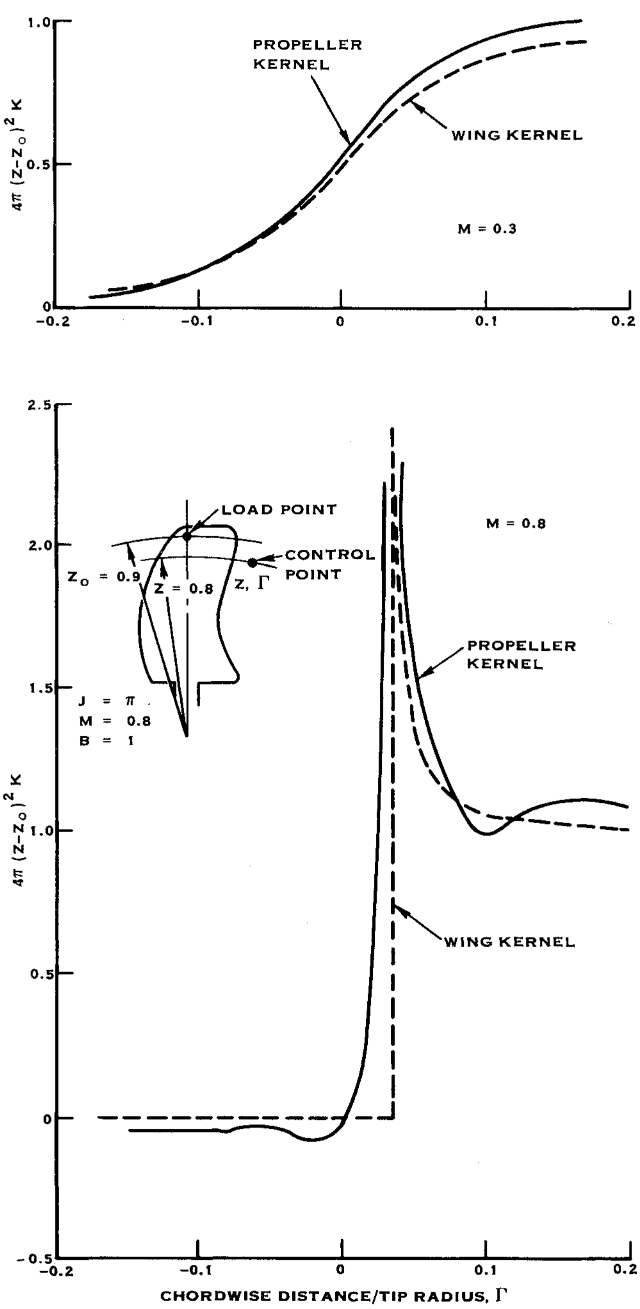

Fig. 5 Wing and propeller kernel functions compared with load and control points close together.

The fourth term is even in $(\Gamma/\sigma-\Gamma_0/\sigma_0)$ and also decays far upstream and downstream. It has no analog in the subsonic wing kernel of Eq. (4a), which contains only terms that are constant and odd with respect to $\Gamma-\Gamma_0$. However, this term is required to mimic the behavior of the supersonic wing kernel, where the upwash pattern is shifted back along Mach lines. Note that this term is zero for incompressible flow because the integration range $1/(1+M)<k<1/(1-M)$ vanishes.

Computed Kernel Function Trends

The general behavior of the kernel described above in analytical terms will now be demonstrated with numerical calculations of Eq. (5). Despite the formidable appearance of

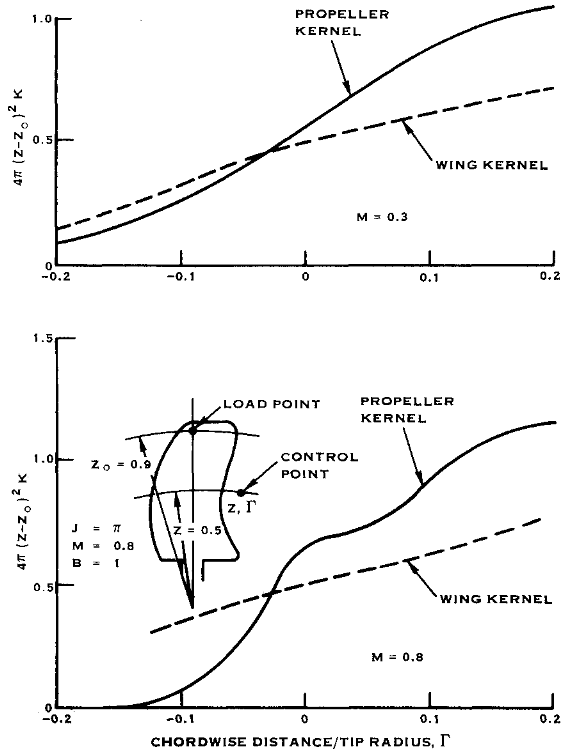

Fig. 6 Wing and propeller kernels compared with load and control points further apart.

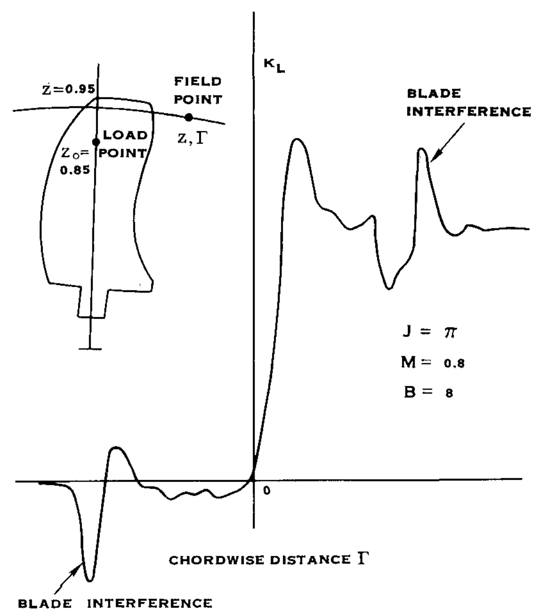

Fig. 7 Kernel calculation for point loads showing effects of blade interference. Compare with Fig. 5, which was calculated for $B=1$.

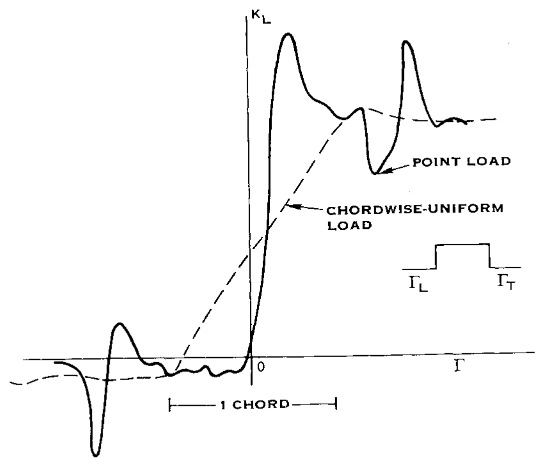

Fig. 8 Smoothing of the induced field when load is distributed rather than concentrated at a point.

this function, it can be computed efficiently by taking advantage of two facts. First, there are asymptotic forms of the Bessel functions that can be subtracted from various terms in Eq. (5) to accelerate convergence of the sums and integrals. When these forms are added back, they can be integrated and summed analytically. Second, the integrals in Eq. (5) are Fourier sine and cosine transforms in the streamwise coordinate $(\Gamma(\sigma-\Gamma_0/\sigma_0)$. Thus, by using fast Fourier transform algorithms, the entire curve of K_L vs $(\Gamma/\sigma-\Gamma_0/\sigma_0)$ can be generated as an array in one pass. The curves in this section are presented for load points at (or centered at) $\Gamma_0=0$.

Because the radial integration has not yet been performed, the kernel function represents the flowfield of the horseshoe vortex sketched in Fig. 4 whose bound section has collapsed to zero length. Figure 5 demonstrates that the kernel for a one-bladed propeller is similar to the wing kernels for control (or field) points close to the load (or source) point. The incompressible calculation, at the top in the figure, shows the smooth upwash behavior expected from Eq. (4a). It also exhibits the familiar property that the induced flow at the source point is ½ and final wake value. The compressible flow condition, represented at the bottom of Fig. 5, is similar to the design point for the SR-3 propfan shown in Fig. 2. The wing kernel from Eq. (4b) shows a square-root singularity at the Mach wave and zero induction ahead of the Mach wave. The propeller kernel behaves similarly except that it does not quite equal zero ahead of the Mach cone. Note that it was necessary to use different formulas for the wing kernel in subsonic and supersonic flow; however, the propeller kernel was calculated with the same formula for both portions of Fig. 5.

From the results shown in Fig. 5, it might be tempting to use the wing kernel for propeller calculations. However, this would not be satisfactory for several reasons. First, the magnitudes of curves in Fig. 5 are dominated by the $(z-z_0)^{-2}$ singularity. When this singularity is integrated out, it produces an effect roughly equal in magnitude to that of the underlying nonsingular terms. Other reasons are given in the next two figures. Figure 6 shows, for source and control points further apart, that the wing and propeller kernels are decidedly different. Also, blade interference effects, shown in Fig. 7, have a powerful effect at high Mach numbers.

Figure 7 was computed for a point load, which is useful for illustrating the mathematical behavior of K_L. However, point load representations are undersirable in supersonic flow because of the rapid upwash variations that are predicted. When the load is properly distributed over the chord, the rapid variations are considerably smoothed out. This is easy to demonstrate because K_L can be integrated analytically over a constant chordwise load. The analytical procedure will be

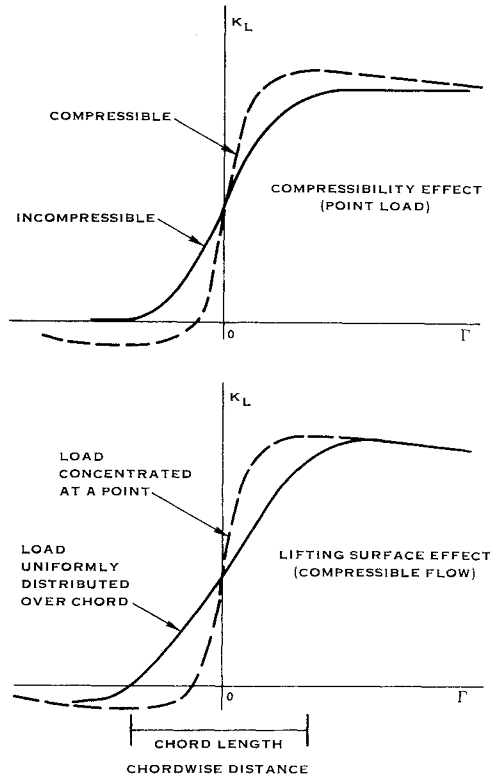

Fig. 9 Effects on induced flowfield of compressibility and distributed chord; $M=0.8$, $J=\pi$, $z=0.65$, $z_0=0.55$.

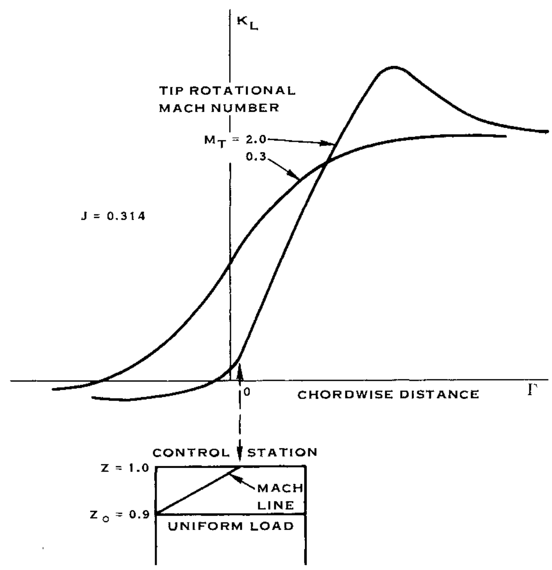

Fig. 10 Sweep back of induced field along Mach line.

described in the next section but the result for a chord-to-diameter ratio of 0.15 is shown in Fig. 8. It can be seen that the rapid chordwise variations caused by blade interference and Mach waves are drastically reduced.

Figure 9 illustrates two interesting effects which relate to the use of incompressible lifting line induction methods for wide chord blades at high subsonic speeds. At the top are curves calculated compressibly and incompressibly for a point load (as in lifting line theory). As might be expected, the effect of compressibility is to steepen the disturbance wavefront. A lifting line theory would use the $\Gamma=0$ value from the curve in the induction calculation for an unswept blade. The figure shows that incompressible theory would be perfectly adequate for this case. However, for a swept blade, a K_L value for $\Gamma>0$

would be needed. In this case, a substantial error arises from use of incompressible theory. In the lower portion of Fig. 9, the lifting surface effect (distributed chord vs lifting line) is illustrated for the compressible condition above. It can be seen that the effect of spreading out the source is to spread out the induction. Again, good accuracy is obtained only for unswept blades where the $\Gamma=0$ value would be used. Ironically, the compressibility and lifting surface effects tend to compensate in the swept blade case. This may partly explain why the simplified induction methods currently in use have been successful for design of first-generation propfan models.

It has been stated[1] that, from a mathematical point of view, the problem addressed here is subsonic and, therefore, there can be no zones of silence in the flowfield. After all, an observer in front of the propeller will hear it, so long as the flight speed is subsonic. But intuitively, we know that, near the load point, disturbances must be swept back along Mach lines. This behavior is illustrated in Fig. 10 by a chordwise-uniform load distribution. It can be seen that the induction pattern moves back with increasing Mach number, as required. As was shown in Fig. 5, the "zone of silence" is not absolute.

Lift Calculation Method

Equation (2) cannot be inverted analytically so that resort must be made to a numerical method analogous to those used in wing theory. These procedures generally discretize the load representation in some manner so that the equation can be inverted by matrix methods. The flow tangency boundary condition is enforced at a number of control points on the blade surface equal to the number of load elements. Typical load representations include constant pressure panels, constant load line segments (analogous to horseshoe vortices in vortex methods), and pressure mode series. For subsonic wings, all of these have been used by various investigators with good success. For supersonic flow, greater care must be taken because discrete load elements induce flow distributions that fluctuate rapidly near Mach lines from the source edges. This leads to calculated results that can be abnormally sensitive to control point location. Some supersonic wing methods are based on special chordwise modes whose shapes are calculated using wing geometries where exact solutions are available. Since there are no such solutions for propellers, it was felt that the first load representation should be general with respect to chordwise and spanwise variation to allow it to adjust for features such as blade interference and tip effects. Also, the representation had to have no edges or corners (except at the tip) that would lead to the control point sensitivity mentioned above. The system arrived at is shown in Fig. 11. The blade surface is divided into a number of spanwise panels whose widths are a constant percentage of the local chord. A lift force distribution is centered at the one-quarter chord of each of the panels and control regions are centered at the three-quarter chord point of each panel. The spanwise load variation is given by a series, each term of which R_j is continuous and varies as wing loading at the tip:

$$R_j = z_0^j \sqrt{1-z_0^2} \tag{7}$$

The lift elements are not concentrated on lines but are distributed somewhat in the chordwise direction with a Gaussian smearing function that provides a more realistic pressure variation and helps converge the integrals in the kernel function more rapidly. Similarly, flow tangency is enforced, not at a point, but in an average sense over a chordwise region centered at the three-quarter chord points of the panels. This verbal description will be made specific with the mathematical description below.

In the following paragraphs, the integral equation [Eq. (2)] will be approximated in discrete form as

$$\bar{W}_\mu = \sum_\nu L_\nu \bar{K}_{\mu\nu} \tag{8}$$

where the $\bar{K}_{\mu\nu}$ are integrated kernel function elements, $\bar{W}_\mu$ downwash angles computed at the control points, and L_ν load coefficients to be found by inverting the matrix of $\bar{K}_{\mu\nu}$. To keep track of the various control and load elements, the index system given below was adopted.

Control points:

radii $\quad z=z_i; \quad i=1,2,\ldots,$ NSM

chordwise stations $\quad \Gamma=\Gamma_{\bar{m}}; \quad \bar{m}=1,2,\ldots,$ NCP

Load indices:

radial modes $\quad R_j(z_0); \quad j=1,2,\ldots,$ NSM

chordwise locations $\quad \Gamma_0=\Gamma_{0\bar{n}}; \quad \bar{n}=1,2,\ldots,$ NCP

where NCP is the number of chordwise panels and NSM the number of spanwise modes. Thus, load and control point indices that combine chordwise and spanwise effects for Eq. (8) are:

$$\mu=(i-1)\mathrm{NCP}+\bar{m}=1,2,\ldots,\mathrm{NCP}\cdot\mathrm{NSM} \tag{9}$$

$$\nu=(j-1)\mathrm{NCP}+\bar{n}=1,2,\cdots,\mathrm{NCP}\cdot\mathrm{NSM} \tag{10}$$

The lift pressure distribution for Eq. (1) now can be written as

$$\Delta C_p(\Gamma_0,z_0) = \sum_{j,\bar{n}} L_\nu R_j(z_0) C_{\bar{n}}(\Gamma_0,z_0) \tag{11}$$

where $C_{\bar{n}}$ are chordwise shape factors whose amplitudes will be chosen for normalization: $\int C_{\bar{n}} \mathrm{d}\Gamma_0 = 1$.

To establish the detailed form of Eq. (8), we define the Gaussian weighting function which centers the control region at $\Gamma_{\bar{m}}$:

$$G_{\bar{m}}(\Gamma,z) = \frac{2\sqrt{\ell n 2}}{\Delta\sqrt{\pi}} \exp\left[-\frac{4\ell n 2}{\Delta^2}(\Gamma-\Gamma_{\bar{m}})^2\right] \tag{12}$$

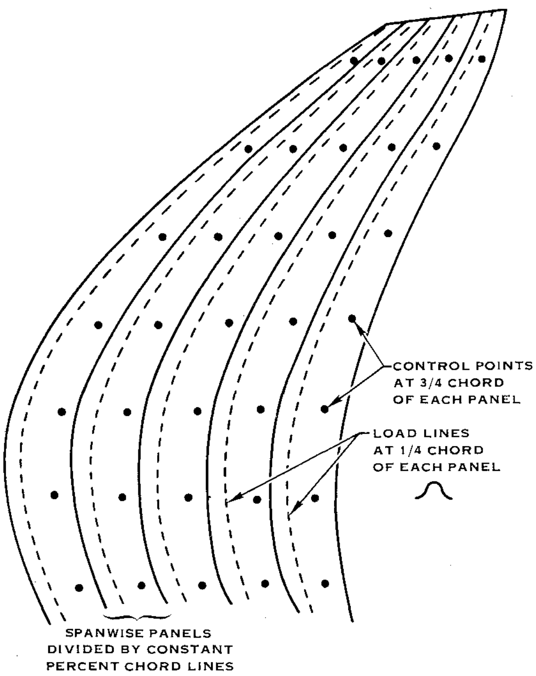

Fig. 11 Load discretization method and control point location.

and operate on both sides of Eq. (2) as follows:

$$W'_{\hat m}(z) = \int G_{\hat m}(\Gamma,z)\,\alpha_i(\Gamma,z)\,\mathrm{d}\Gamma$$
$$= \iint \Delta C_p(\Gamma_0,z_0) \int G_{\hat m}(\Gamma,z) K_L(\Gamma,z,\Gamma_0,z_0)\,\mathrm{d}\Gamma\,\mathrm{d}\Gamma_0\,\mathrm{d}z_0 \tag{13}$$

Then the load description of Eq. (11) is inserted into Eq. (13) and the control point radii, $z=z_i$, are selected to give

$$W'_{\hat m}(z_i) = \sum_{j,\hat n} L_\nu \int R_j(z_0) K_{\hat m,\hat n}(z_i,z_0)\,\mathrm{d}z_0 \tag{14}$$

where

$$K_{\hat m\hat n}(z_i,z_0) = \iint K_L(\Gamma,z;\Gamma_0,z_0) G_{\hat m}(\Gamma,z_i) C_{\hat n}(\Gamma_0,z_0)\,\mathrm{d}\Gamma_0\,\mathrm{d}\Gamma \tag{15}$$

And finally, by identifying $W_\mu = W'_{\hat m}(z_i)$, we arrive at Eq. (8) with

$$\bar K_{\mu\nu} = \int_{z_h}^{1} R_j(z_0) K_{\hat m\hat n}(z_i,z_0)\,\mathrm{d}z_0 \tag{16}$$

With a Gaussian load distribution function

$$C_{\hat n}(\Gamma_0,z_0) = \frac{2\sqrt{\ln 2}}{\Delta_0\sqrt{\pi}} \exp\left[-\frac{4\ln 2}{\Delta_0^2}(\Gamma_0-\Gamma_{0\hat n})^2\right] \tag{17}$$

the double integration of Eq. (15) can be done analytically. The result is

$$K_{\hat m\hat n} = \frac{Bz_0 z\sigma_0 a^4}{4\pi^2\sigma^2}\int_0^\infty \bar X_0\cdot\bar X\, kI_0(a\beta z_< k)K_0(a\beta z_> k)\sin\left[a\left(\frac{\Gamma}{\sigma}-\frac{\Gamma_0}{\sigma_0}\right)k\right]\mathrm{d}k$$
$$+\frac{B^3\sigma_0^3}{4\pi z_0 z}\sum_{m=1}^{\infty} m^2 I_{mB}(mBaz_<)K_{mB}(mBaz_>)$$
$$-\frac{B^3\sigma_0}{8\pi\sigma^2 z_0 z}\sum_{m=1}^{\infty} m^2\int_{-\infty}^{\infty}\bar X_{0m}\cdot\bar X_m\frac{1}{k}[a^2z_0^2(k-1)-1][a^2z^2(k-1)-1](JY)_{mB}\sin\left[mBa\left(\frac{\Gamma}{\sigma}-\frac{\Gamma_0}{\sigma_0}\right)k\right]\mathrm{d}k$$
$$-\frac{B^3\sigma_0}{8\pi\sigma^2 z_0 z}\sum_{m=1}^{\infty} m^2\int_{[1/(1+M)]}^{[1/(1-M)]}\bar X_{0m}\cdot\bar X_m\frac{1}{k}[a^2{z_0}^2(k-1)-1][a^2z^2(k-1)-1](JJ)_{mB}\cos\left[mBa\left(\frac{\Gamma}{\sigma}-\frac{\Gamma_0}{\sigma_0}\right)k\right]\mathrm{d}k \tag{18}$$

where

$$\bar X_0 = \exp\left[-\left(\frac{a\Delta_0 k}{4\sqrt{\ln 2}\,\sigma_0}\right)^2\right],\quad \bar X = \exp\left[-\left(\frac{a\Delta k}{4\sqrt{\ln 2}\,\sigma}\right)^2\right] \tag{19}$$

$$\bar X_{0m} = \exp\left[-\left(\frac{mBa\Delta_0 k}{4\sqrt{\ln 2}\,\sigma_0}\right)^2\right],\quad \bar X_m = \exp\left[-\left(\frac{mBa\Delta k}{4\sqrt{\ln 2}\,\sigma}\right)^2\right] \tag{20}$$

and Δ_0 and Δ are the widths at the one-half amplitude points of the Gaussian functions $C_{\hat n}$ and $G_{\hat m}$.

The radial integration of Eq. (16) is accomplished in a fashion similar to the spanwise integrals in many existing wing methods. As shown in Fig. 12, the integration range is divided into three ranges, one of which contains the singularity at $z_0=z_i$. In the nonsingular regions, the integration is performed using a trapezoidal method with step sizes equal to 1% of the tip radius. Integration through the singular region is performed accurately by exploiting the exact form of the singularity that can be derived from Bessel function asymptotic forms. The singular part of the kernel is integrated using the 10-point Lagrange scheme given by Cunningham[6] for the $(z-z_0)^{-2}$ term and the corresponding 10-point form for the $(z-z_0)^{-1}$ term. The nonsingular part in the singular region is integrated using a Lagrange-type curve fit through four points which do not include $z_0=z_i$.

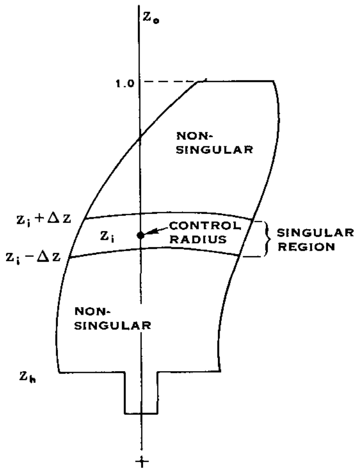

Fig. 12 Division of radial integration range into singular and nonsingular regions.

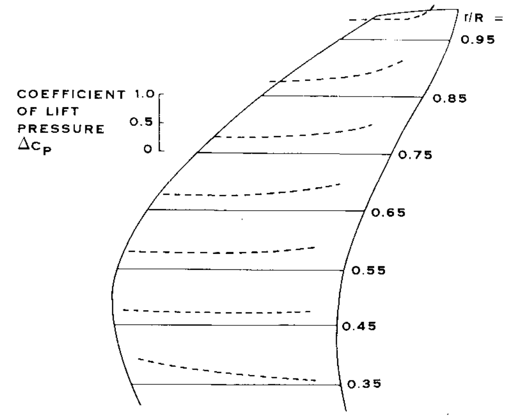

Fig. 13 Lift pressure prediction at SR-3 design points; $M=0.8$, $J=3.057$, $C_P=1.695$.

Drag and Efficiency

The theory presented above predicts lift forces acting normal to the local direction of motion. Since this condition by itself would require zero work, the various drag components now must be considered

In analogy with wing theory, drag and lift coefficients in this paper refer to a resolution of forces parallel and perpendicular to the local direction of motion. However, to compute propeller thrust and power, forces must be resolved into thrust and torque components. This gives the usual equations[7] for elements of thrust coefficient C_T and power coefficient C_P which, in the present notation, are

$$\frac{\mathrm{d}C_T}{\mathrm{d}z} = \frac{1}{4}B\sigma J^2 B_D C_L\left(az-\frac{C_D}{C_L}\right) \tag{21}$$

$$\frac{dC_P}{dz} = \frac{1}{4} B\sigma J^3 B_D C_L az\left(1 + az\frac{C_D}{C_L}\right) \tag{22}$$

where C_D is the section drag coefficient (to be discussed below) including all drag components. Thrust and power coefficients are computed by integrating Eqs. (21) and (22) over the radius.

Apparent efficiency as given by

$$\eta = (C_T/C_P)J \tag{23}$$

includes the effect on C_T of the flow retardation caused by the nacelle. Note that for $C_D = 0$, the above equations give $\eta = 1$.

Drag is expressed as the sum of three components:

$$\frac{C_D}{C_L} = \left(\frac{C_D}{C_L}\right)_F + \left(\frac{C_D}{C_L}\right)_W + \left(\frac{C_D}{C_L}\right)_V \tag{24}$$

where the subscripts denote friction drag, wave drag, and vortex (or induced) drag, respectively. The current treatment of these terms is as follows.

Friction drag is looked up in two-dimensional airfoil tables as a function of C_L with section camber, thickness, and a Mach number adjusted via simple sweep theory. Wave drag is given by the radiated acoustic energy. But, since experimental data for propfans with swept blades shows the acoustic power to be a negligible fraction of shaft power, wave drag is neglected in the calculations below.

Vortex drag is computed by adapting methods given by Ashley and Landahl[5] for wings at subsonic and supersonic speeds where the lift force acts normal to the flight direction. For propellers, this force acts normal to the advance helix and produces a trailing vortex system as a secondary effect. The associated drag (drag due to lift) is computed by determining the kinetic energy per unit length of the far wake. This approach is ideal for propfans because the kinetic energy integral for the far wake

$$T = -\frac{\rho_0}{2} \oiint_{\text{vortex sheets}} \Delta\phi \; w \; ds \tag{25}$$

is exactly the same for subsonic and supersonic blade section speeds. The analogous result for subsonic and supersonic wings is well known (see, for example, Ref. 5, pp. 136 and 175). In Eq. (25), the jump in velocity potential $\Delta\phi$ across a vortex sheet is simply the circulation at the corresponding radius on the blade determined by the lift calculation method of the preceding section. w is the velocity induced normal to the vortex sheet. Evaluation of Eq. (25) for helicoidal sheets proceeds in the same fashion as for wing theory and leads to the same result.

$$\left(\frac{C_D}{C_L}\right)_V = -\frac{1}{2}\frac{w}{U} = -\frac{1}{2}\alpha_{\text{wake}} \tag{26}$$

The downwash angle in the far wake is computed from Eq. (2) with the far wake form of the kernel, which, as noted above, is just twice the second term in Eq. (5).

By combining these equations and recognizing that $\int \Delta C_p \, d\Gamma = 2B_D C_L$, we find

$$\left(\frac{C_D}{C_L}\right)_V = -\int_{z_n}^{1} 2B_D C_L \frac{B^3\sigma_0^3}{4\pi z_0 z} \sum_{m=1}^{\infty} m^2 I_{mB}(mBaz_<) \times K_{mB}(mBaz_>)\,dz_0 \tag{27}$$

As with the Goldstein propeller theory,[8] Eqs. (26) and (27) relate induced velocities and blade loading. The Goldstein theory gives the loading for only the optimum case—constant axial induction along the span. The present theory is more general; it gives the induction distribution for any loading. To verify the theory, Eq. (27) was evaluated with a Goldstein optimum loading for $B_D C_L$. The induction matched Goldstein's.

In summary, propeller drag and efficiency are computed using Eqs. (21-24) and (27) given the C_L distribution obtained from Eq. (14). The radial integration is handled with the methods described at the end of the previous section. In particular, singularities in the integrand of Eq. (27) are integrated using exact sums of the asymptotic forms of the Bessel functions. The nonsingular terms are integrated numerically.

Lift and Performance Calculations

The condition chosen for calculating the distribution of lift pressure was the design point for the SR-3 propfan (shown in Fig. 2) which was tested in the 8×6 ft wind tunnel at NASA Lewis.[9] The design point was for a cruise Mach number of 0.8, an advance ratio $J = 3.057$, and a power coefficient $C_P = 1.695$. This exact point was never tested but crossplots of nearby data points indicate that the desired C_P would have been achieved by setting blade angle to 61.7 deg. To establish the boundary conditions for program input, a finite element structural model of the blade was stored in the computer system. This was "rotated" about the pitch change axis to a blade angle of 61.7 deg and "cut" by 20 concentric cylinders with radii up to the tip radius. The resulting airfoil sections were then unwraped (or laid out flat), the camber lines were constructed, and their slopes were measured with respect to the advance helicoid. This gave the boundary conditions, W_μ in Eq. (8), except for an adjustment required for blockage caused by the spinner, centerbody, and nacelle. The blockage was computed with a compressible streamline curvature code, converted to effective changes in air angles, and added to W_μ. The blockage effectively changed the section incidence angles from 2.4 deg at the root to −1.0 deg at the tip. Also, an

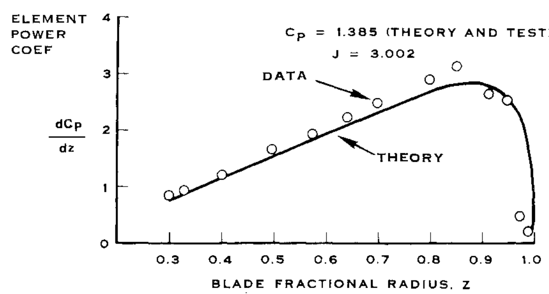

Fig. 14 Comparison of experimental and theoretical power distributions (SR-3 propfan).

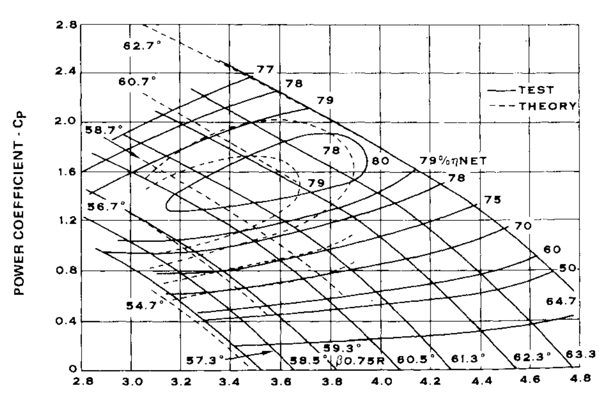

Fig. 15 Comparison of theoretical and experimental performance maps at $M = 0.8$.

estimate of blade twist change due to dynamic effects was used to modify the blade angle input.

For the calculations, five panels were selected as shown in Fig. 11 with control areas at 7 radii: $z = 0.35, 0.45, \ldots, 0.95$. This gave a total of 35 control areas which were centered at the three-quarter chord points of the panels. Loads were distributed along the one-quarter chord points of the panels and were described by seven terms of the series given in Eq. (7). As described in conjunction with Eqs. (12) and (17), both the control and load regions are smeared in the chordwise direction by amounts corresponding to one-quarter of a panel width.

The computed distribution of lift pressure is shown in Fig. 13. Chordwise distributions are shown to be fairly flat, as is desired for both noise and performance.

Unfortunately, there are no pressure data to verify the calculations shown in Fig. 13. The most detailed measurements available[9] are from wakes behind the rotor whose readings can be interpreted in terms of the radial distribution of power coefficient dC_P/dz. This distribution is given in Fig. 14 for the test point nearest the SR-3 design point. The agreement with test shown in Fig. 14 is very encouraging and indicates that spanwise load distributions can be computed with some confidence with this method. However, it must be noted for both Figs. 13 and 14 that the overall blade angle was reduced in the calculations by 2 deg from the test values to achieve the power measured in the test.

Finally, entire performance maps were generated and compared with wind tunnel data. The sample shown in Fig. 15 for Mach 0.8 is in good agreement with data even over a range of off-design conditions. Maps at $M = 0.45$, 0.6, 0.7, and 0.85 showed similar agreement.

By taking advantage of fast Fourier methods and asymptotic forms for Bessel functions, computer time for the lifting surface method has been reduced to a very acceptable level. Computation of the lift distribution in Fig. 13 ran 8 min of CPU time on an IBM 370 computer. Kernel function arrays and inverse matrices can be stored so that new planforms (at the same advance ratio, Mach number, and number of blades) can be run for about 1 min of CPU time. Retwists and recambers for the same planform run about 1 s.

Summary and Conclusions

A new lifting surface integral equation theory for propeller steady aerodynamics has been presented that generalizes wing kernel function theories to include effects of rotation and multiple blades. Within the limitations of linearization, it accounts rigorously for effects of sweep, three dimensionality, blade interference, and compressibility. The kernel function is valid in a single form for the condition, typical of propfans, where the blade section relative speeds are subsonic at the roots and supersonic at the tips.

The kernel function was shown to exhibit the proper behavior with respect to singularities and, in the far wake limit, was found to include the classic Goldstein[6] results as a special case. Although the kernel is a complicated expression, it is convenient for analytical work because it can be integrated analytically in the chordwise direction. Spanwise integrals can be done accurately because the singularity at the load point has been extracted analytically.

The integral equation was inverted using a method that is new but similar to those used in wing theory. Also, vortex (or induced) drag is computed by a technique adapted from wake methods well known in wing analysis. The theoretical performance maps are in good agreement with data at flight Mach numbers up to 0.85. Furthermore, the spanwise load distribution compares well with values determined from downstream wake measurements.

References

[1] Hanson, D. B., "Compressible Helicoidal Surface Theory for Propeller Aerodynamics and Noise," *AIAA Journal*, Vol. 21, June 1983, pp. 881-889.

[2] Jou, W. H., "Finite Volume Calculations of Three-Dimensional Flow Around a Propeller," AIAA Paper 82-0957, June 1982.

[3] Bober, L. J., Kutler, P., and Chausee, D. S., "Prediction of High Speed Propeller Flow Fields Using a Three-Dimensional Euler Analysis," AIAA Paper 83-0188, Jan. 1983.

[4] Bisplinghoff, R. L. and Ashley, H., *Principles of Aeroelasticity*, John Wiley & Sons, New York, 1962.

[5] Ashley, H. and Landahl, M. T., *Aerodynamics of Wings and Bodies*, Addison-Wesley Publishing Co., Reading, Mass., 1965.

[6] Cunningham, H. J., "Improved Numerical Procedure for Harmonically Deforming Lifting Surfaces from the Supersonic Kernel Function Method," *AIAA Journal*, Vol. 4, Nov. 1966, pp. 1961-1968.

[7] Dommasch, D. O., *Elements of Propeller and Helicopter Aerodynamics*, Pitman Publishing Corp., New York, 1953.

[8] Goldstein, S., "On the Vortex Theory of Screw Propellers," *Proceedings of the Royal Society*," Vol. A-123, 1929, pp. 440-465.

[9] Rohrbach, C. et al., "Evauation of Wind Tunnel Performance Tests of Advanced 45 deg Swept Eight-Bladed Propeller at Mach Numbers from 0.45 to 0.85, Final Report for Contract NAS3-20769," Feb. 1981.